HHS Public Access

Author manuscript

Dev Biol. Author manuscript; available in PMC 2023 July 27.

Published in final edited form as:

Dev Biol. 2023 July ; 499: 75–88. doi:10.1016/j.ydbio.2023.04.006.

CFAP45, a heterotaxy and congenital heart disease gene, affects cilia stability

E. Deniz[a,*], **M. Pasha**[a], **M.E. Guerra**[a], **S. Viviano**[a], **W. Ji**[a], **M. Konstantino**[a], **L. Jeffries**[a], **S.A. Lakhani**[a], **L. Medne**[b], **C. Skraban**[b], **I. Krantz**[b], **M.K. Khokha**[a,c,**]

[a]Pediatric Genomics Discovery Program, Department of Pediatrics, Yale University School of Medicine, 333 Cedar Street, New Haven, CT, 06510, USA

[b]Department of Pediatrics, Division of Human Genetics, Children's Hospital of Philadelphia, USA

[c]Department of Genetics, Yale University School of Medicine, 333 Cedar Street, New Haven, CT, 06510, USA

Abstract

Congenital heart disease (CHD) is the most common and lethal birth defect, affecting 1.3 million individuals worldwide. During early embryogenesis, errors in Left-Right (LR) patterning called Heterotaxy (Htx) can lead to severe CHD. Many of the genetic underpinnings of Htx/CHD remain unknown. In analyzing a family with Htx/CHD using whole-exome sequencing, we identified a homozygous recessive missense mutation in *CFAP45* in two affected siblings. CFAP45 belongs to the coiled-coil domain-containing protein family, and its role in development is emerging. When we depleted Cfap45 in frog embryos, we detected abnormalities in cardiac looping and global markers of LR patterning, recapitulating the patient's heterotaxy phenotype. In vertebrates, laterality is broken at the Left-Right Organizer (LRO) by motile monocilia that generate leftward fluid flow. When we analyzed the LRO in embryos depleted of Cfap45, we discovered "bulges" within the cilia of these monociliated cells. In addition, epidermal multiciliated cells lost cilia with Cfap45 depletion. Via live confocal imaging, we found that Cfap45 localizes in a punctate but static position within the ciliary axoneme, and depletion leads to loss of cilia stability and eventual detachment from the cell's apical surface. This work demonstrates that in *Xenopus,* Cfap45 is required to sustain cilia stability in multiciliated and monociliated cells, providing a plausible mechanism for its role in heterotaxy and congenital heart disease.

Keywords

Congenital heart disease; Heterotaxy; CFAP45; Cilia; *Xenopus*

*Corresponding author: engin.deniz@yale.edu (E. Deniz). **Corresponding author. Pediatric Genomics Discovery Program, Department of Pediatrics, Yale University School of Medicine, 333 Cedar Street, New Haven, CT, 06510, USA. mustafa.khokha@yale.edu (M.K. Khokha).

Declaration of competing interest

SAL and MKK are co-founders of Victory Genomics, Inc.

Appendix A. Supplementary data

Supplementary data to this article can be found online at https://doi.org/10.1016/j.ydbio.2023.04.006.

1. Introduction

Congenital heart disease (CHD) is the most common birth defect, affecting ~1% of live births and 10% of aborted fetuses worldwide (Hoffman and Kaplan, 2002). Recent genomic studies in CHD patients suggest a genetic basis (Zaidi et al., 2013; Homsy et al., 2015; Sifrim et al., 2016; Pierpont et al., 2007), yet, these studies demonstrate high locus heterogeneity, and most of the candidate genes identified in these studies do not have a plausible mechanism for pathogenesis. Therefore, there is a pressing need to understand the role of these candidate genes in cardiac development to improve our ability to care for affected children, provide genetic counseling, and better understand cardiac development.

A severe form of CHD can result from heterotaxy (Htx), a disorder of left-right (LR) patterning characterized by the abnormal arrangement of the internal organs across the LR axis. The heart has critical LR asymmetries, and mispatterning of the LR axis can severely disrupt cardiac function. Near the end of gastrulation, a conserved structure, the Left-Right Organizer (LRO), is formed. The LRO breaks LR symmetry to establish laterality (Basu and Brueckner, 2008; Hamada Nakanishi et al., 2016). The LRO is known as the ventral node in mice (Basu and Brueckner, 2008), Hensen's node in chicken (Charrier et al., 1999), the gastrocoel roof plate (GRP) in frogs (Schweickert et al., 2007), and Kupffer's vesicle in fish (Essner et al., 2005). In the LRO, motile monocilia, polarized along the anterior-posterior (AP) axis, beat to create leftward extracellular fluid flow sensed by the immotile cilia (McGrath et al., 2003; Yoshiba et al., 2012; Boskovski et al., 2013). Once the flow is sensed at the left margin of the LRO, *dand5* (formerly *coco* in *Xenopus*, *Cerl2* in mouse, and *charon* in zebrafish), a nodal antagonist, is down-regulated on the left, leading to *smad-2* signaling on the left side (Schweickert et al., 2010; Vonica and Brivanlou, 2007; Kawasumi et al., 2011). Subsequently, *pitx2*c is activated in the left lateral plate mesoderm. This asymmetry at the lateral plate mesoderm results in normal asymmetric organogenesis, whereas a failure in proper LR patterning can lead to heterotaxy and congenital heart disease (Bowers et al., 1996). Therefore, proper cardiac development relies on cilia function.

Left-right patterning can be readily analyzed in the frog *Xenopus* by observing cardiac looping through its transparent tadpole skin (Blum and Vick, 2015; Sempou and Khokha, 2019; Deniz et al., 2018). In normal *situs*, the outflow tract of the heart bends to the right (a D-loop), whereas in abnormal states, either the outflow tract loops entirely to the opposite side (an L-loop) or remains midline (an A-loop). Furthermore, earlier steps of the LR signaling cascade can be easily analyzed in *Xenopus*, from cilia signaling in the LRO to asymmetric *dand5* and *pitx2c* expression to asymmetric organogenesis. With these advantages, *Xenopus* is widely used to study LR patterning and candidate CHD genes (Sempou and Khokha, 2019).

Here, we present the case of two siblings in a family with severe CHD/Htx. By whole-exome sequencing, both children had rare homozygous recessive mutations in the *CFAP45* gene (CCDC19 - Coiled-Coil Domain Containing 19; *NESG1*-Nasopharyngeal Epithelium Specific Protein 1). CFAP45 belongs to the coiled-coil domain-containing protein family that contains other proteins previously associated with heterotoxy, including CCDC11 (Narasimhan et al., 2015), CCDC39, and CCDC40 (Antony et al., 2013; Becker-Heck

et al., 2011). Recently two reports described the potential role of CFAP45 in ciliary function yet fundamentally proposed different roles. Dougherty et al. linked CFAP45 to cilia motility, where they showed the proteomic profiling linking CFAP45 to dynein ATPase components and showed the expression of *Cfap45* in mouse LRO. Interestingly despite significant motility defects, the ultrastructure of the respiratory cilia from CFAP45 deficient individuals and *Cfap45* −/− sperm was indistinguishable from healthy controls (Dougherty et al., 2020). In contrast to this report, Owa et al., using cryo-electron tomography and high-speed atomic force microscopy in Chlamydomonas, characterized the ortholog FAP45 as an inner microtubule protein essential for ciliary stabilization, questioning the proposed role of CFAP45 in ciliary motility (Owa et al., 2019).

In the light of these studies, using our *Xenopus* model, we first provide evidence for pathogenicity by demonstrating that the *CFAP45* variant found in this family is detrimental to protein function. We then demonstrate that Cfap45 protein is a static, structural component of the ciliary axoneme and essential for motile cilia stability and proper LR axis patterning during development. Interestingly when *cfap45* is depleted in *Xenopus,* similar to the previous report by Dougherty et al., ciliogenesis in the multiciliated epithelium of the *Xenopus* epidermis is not initially affected. However, in *Xenopus* multiciliated cells, the axoneme could not withstand the beating forces in contrast to this report. Over a short period, cilia destabilized and shed from the epidermal surface, suggesting the role of Cfap45 in cilia stabilization.

2. Materials and methods

2.1. Xenopus tropicalis husbandry

Xenopus tropicalis were housed and cared for in our aquatics facility according to established protocols approved by the Yale Institutional Animal Care and Use Committee (IACUC) in accordance with NIH guidelines. Ovulations and IVFs were performed as previously described (Lane and Khokha, 2022).

2.2. Genome editing and microinjections

Microinjections of *Xenopus* embryos were performed per standard protocols (Deniz et al., 2017). Briefly, 1.0 mm borosilicate glass needles (World Precision Instruments) were used to inject embryos at the one-cell stage with either 2–10 ng of splice morpholino oligo (MO) spanning exon 2 and intron 2 (5′-TAAGGCCCCATATTCCTCACCTTCA-3′, GeneTools) or 600 pg of sgRNA plus 1.5 ng of Cas9 protein (PNA Bio) for knockdown experiments. Doses for one-of-two-cell injections were half of those for one-cell injections.

To make G0 CRISPR mutants, we generated sgRNAs using the EnGen sgRNA synthesis kit (NEB) following the manufacturer's instructions using the following oligos:

- CRISPR#1: GTCGCACAGAAGAACCCCAACGG – targeting Exon2 of *cfap45*
- CRISPR#2: TGCTCGGGTGTTGACCAAAGAGG – targeting Exon3 of *cfap45*

Injections were traced with either 90 pg of membrane RFP (Gong et al., 2004) or Dextran Alexa Fluor 488 (Invitrogen). Full-length human *CFAP45* (clone HsCD00515731) was

subcloned into the pCSDest2, pCS-EGFP-Dest, and pCS-cherry-Dest vector using Gateway recombination techniques. To create mutants, site-directed mutagenesis was conducted on wild-type human *CFAP45* according to standard methods using the Q5 Site-Directed Mutagenesis Kit (New England BioLabs) (Lek et al., 2016). Primers (available on request) were designed for the patient variant, and the nucleotide change was confirmed through Sanger sequencing. Capped mRNAs were generated *in vitro* by linearizing using appropriate restriction enzymes and transcribing with the mMessage machine kit (Ambion), following the manufacturer's instructions. Post-injections, embryos were flooded with 3% Ficoll in 1/9x MR. They were left to rest for at least 1 h (preferably at 28 °C when employing CRISPR/Cas9 to maximize Cas9 activity) before being transferred to a dish containing 1/9x MR with 50 μg/ml of gentamicin and incubated at 22–26 °C along with sibling control embryos. Injections were confirmed by fluorescent lineage tracing with a Zeiss Lumar fluorescence stereomicroscope the day after injection, and tadpoles were incubated until the needed stage.

2.3. Inference of CRISPR editing (ICE) verification

CRISPR efficiency was determined through Sanger sequencing. CRISPR #1 and #2 injected embryos were grown to ~stage 43. Embryos were anesthetized by brief incubation in 0.05% benzocaine, then transferred to individual tubes. Genomic DNA was extracted by immersing in 100 μl of 50 mM sodium hydroxide per embryo, incubating at 95 °C for 10 min, vortexing, then neutralizing by adding 20 μl of 1M Tris pH 7.4. The region around the cut site was amplified using forward primers ~200bp upstream and reverse primers ~500bp downstream

- CRISPR #1 forward: 5′-GGGATCTTGATGGAATGTCG-3′
- CRISPR#1 reverse: 5′-GCTGCCAGTCTGGTGTCTCT-3′
- CRISPR#2 forward: 5′-CGGTCAGGATGATTGCCTAT-3′
- CRISPR#2 reverse: 5′-GGGTCCTATTTCCCCTAGCA-3′

PCR products were purified, then sent for Sanger sequencing using the forward primer for each. Sequences were analyzed for insertion/deletion efficiency using the online Inference of CRISPR Edits (ICE) tool (Synthego) https://www.synthego.com/products/bioinformatics/crispr-analysis.

2.4. Optical Coherence Tomography imaging

A Thorlabs Ganymede 900 nm spectral domain-OCT Imaging System was used, which allows for 1.4 mm imaging depth in the air + water −2.2 μm Axial Resolution in water. We obtained 2D cross-sectional images by scanning at 36 kHz (36000 A-scans per second). Measurements were obtained with ThorImageOCT software version 4.4.6. To examine cilia-driven extracellular fluid flow across the embryonic epidermis, embryos were raised to stages 23–24, then scanned by OCT to determine the fluid flow speed by tracking the endogenous particles within the vitelline envelope, as previously described (Tang et al., 2019). Embryos were categorized qualitatively as either "normal flow" (when compared to stage-matched controls), "slow flow," which is approximately half of the average flow speed

or less, or “no flow,” which is virtually no particle movement, as previously described (Date et al., 2019).

2.5. Whole mount in situ hybridization

In situ hybridization was performed according to standard protocols (Khokha et al., 2002), except we used ethanol for all dehydration steps and 4% paraformaldehyde + 0.1% glutaraldehyde in PBS for the post-staining fixative for 20 min at room temperature (instead of Bouin’s fixative). DIG-UTP-containing RNA probes were produced using a HiScribe T7 RNA Synthesis Kit (NEB). Linearized plasmids containing the desired insert were used as the template

Gene	Reference sequence	Expression Vector	Linearization Restriction Enzyme
dand5	TEgg007d24	pCS107	ClaI
pitx2c	TNeu083k20	pCS107	HindIII

dand5: Embryos were raised to stage 15 (pre-LRO flow) and stage 18 (post-LRO flow), then fixed in MEMFA for 2 h at room temperature. The embryos were washed for 3 × 15 min with PBS. The LROs were dissected and dehydrated with several washes in 100% ethanol, and then the *in situ* hybridization procedure was executed.

pitx2c: Embryos were raised until stage 28–30, fixed with MEMFA for 4 h at room temperature, dehydrated with several washes in 100% ethanol, then put through the *in situ* hybridization procedure.

2.6. Immunofluorescence and microscopy

2.6.1. Left-Right Organizer—Prior to dissection of LROs, stage 16–17 embryos were fixed with 4% PFA in PBS for 2 h at room temperature, then washed 3 × 15 min with PBS. The LROs were dissected, then incubated in a blocking buffer (3% bovine serum albumin (BSA) in PBS + 0.2% Triton X-100) for 1 h at RT. They were incubated overnight in mouse anti-ADP-ribosylation factor-like protein 13B (Arl13b clone N295B/66, NeuroMab) diluted 1:100 in blocking buffer at 4 °C overnight. The LROs were washed 3 × 15 min with PBS, followed by incubation in anti-mouse Alexa Fluor 488 (Thermo Fisher Scientific) diluted 1:500 in blocking buffer for 2 h at room temperature. Then, specimens were washed 3 × 15 min with PBS and incubated in Alexa Fluor 647 Phalloidin (Thermo Fisher Scientific) diluted 1:100 in blocking buffer for 1 h at RT. The embryos were washed 2 × 10 min with PBS before mounting between two coverslips with ProLong Gold Antifade Mountant (Thermo Fisher Scientific) and imaging with a Zeiss 710 confocal microscope.

2.6.2. Epidermis—Stage 23–24 embryos were screened for particle flow speed within the vitelline membrane, raised to stage 26–28 until they hatched out of the vitelline membrane, then fixed as the LROs above. The embryos were stained as above using mouse anti-acetylated tubulin (Sigma cat. #T6793) diluted 1:1000 as the primary antibody rather than anti-Arl13b. Alternatively, embryos were injected into one of two cells with human

CFAP45 mRNA plus membrane RFP and grown to stage 30–32 when they were fixed and stained with mouse anti-acetylated tubulin. To localize Cfap45, stage 30–32 embryos were fixed as above. Embryos were incubated overnight in a mix of primary antibodies; rabbit anti-CCDC19 (Abcam cat. #ab170230) diluted 1:200 and mouse anti-acetylated tubulin. This was followed by incubation in a mix of secondary antibodies; anti-rabbit Alexa Fluor 488 and anti-mouse Alexa Fluor 594 (Thermo Fisher Scientific), each diluted at 1:500.

2.7. Transmission electron microscopy

Embryos were fixed in 2.5% glutaraldehyde and 2% paraformaldehyde in 0.1M sodium cacodylate buffer pH7.4 for 1 h, rinsed in the buffer, then post-fixed in 1% osmium tetroxide and, en bloc, stained in 2% aqueous uranyl acetate for an additional hour. Then the embryos were rinsed and dehydrated in an ethanol series followed by resin infiltration with Embed 812 (Electron Microscopy Sciences) and baked overnight at 60 °C. Hardened blocks were cut using a Leica UltraCut UC7. 60 nm sections were collected on formvar/carbon-coated grids and contrast stained using 2% uranyl acetate and lead citrate. The sections on grids were viewed with an FEI Tencai Biotwin TEM at 80Kv. Images were taken using Morada CCD and iTEM (Olympus) software.

2.8. Quantification and statistical analysis

All *Xenopus* experiments were performed a minimum of three times, and the numbers stated in the graphs are a composite of multiple experiments. Measurements via OCT Thorlabs software represented by the mean value ± SEM for each group. Two-tailed Student's t-test analysis was used to examine all significant differences between groups as indicated in the figure legends. Significance was determined when the p-value was lower than 0.05.

3. Results

3.1. Clinical history and whole exome sequencing

According to the report, the proband was the second child born to non-consanguineous parents of South Asian descent (Fig. 1A). He was diagnosed at birth with heterotaxy syndrome, including intestinal malrotation, a right gastric bubble on chest X-ray (Fig. 1C), asplenia, complex congenital heart disease notable for a right aortic arch (Fig. 1D), unbalanced right dominant atrioventricular canal defect, pulmonary atresia with multiple aortopulmonary collaterals, bilateral superior vena cavae, left-sided inferior vena cava with possible separate right-sided hepatic drainage, pulmonary veins to the right-sided atrium (Fig. 1E). He underwent stage-1 Norwood procedure soon after birth and then a stage-2 Glenn procedure at three years of age. His course has been complicated by fibrosis of multiple veins. He has also had periods of hypoxia around his cardiac procedures and has developed seizures, which have been managed with antiepileptics. He has a global developmental delay with delayed speech and motor skills. The medical history was also significant for multiple hospitalizations for recurrent respiratory disease and required daily chest physiotherapy for respiratory clearance. Remarkably similar, the older sibling of the index patient presented with asplenia, pulmonary atresia with a single ventricle, and total anomalous pulmonary venous return, also consistent with heterotaxy syndrome. This child died at 25 days of age from complications related to cardiac malformations.

Clinical whole exome sequencing was performed on the proband to identify a possible cause of his heterotaxy. Although no diagnostic variants were found to explain the phenotype, multiple regions of homozygosity (ROH) were identified, spanning a total of 133 MB over six chromosomes, despite the parents having no known consanguinity (Supplemental Table 1). Within an ROH on chromosome 1, we found a rare homozygous recessive variant,1:159842746_A > G, p.(Leu522Pro) in the *CFAP45* gene (Fig. 1B), which has recently been associated with heterotaxy and cilia dysfunction (Dougherty et al., 2020). Both parents were heterozygous for this variant, and the deceased sibling was also homozygous for this variant based on Sanger sequencing.

3.2. Cfap45 depletion leads to left-right axis defects in Xenopus

To test if we could recapitulate a heterotaxy phenotype in an animal model by depleting *cfap45,* we used CRISPR/Cas9 or morpholino oligos (MOs) in the frog *Xenopus tropicalis*. We tested two non-overlapping sgRNAs, CR#1 (CRISPR#1) and CR#2 (CRISPR#2), along with Cas9 protein to deplete *cfap45* and raised tadpoles to stage 46 (st.46) to assess cardiac looping as previously described (Fig. 1F) (del Viso and Khokha, 2012; Bhattacharya et al., 2015). In uninjected control embryos (UIC), only 2% of embryos had abnormal cardiac loops (L or A-loops), with most embryos having a normal D-loop (Fig. 1F and G). On the other hand, *cfap45*-depleted tadpoles exhibited 21% ± 5.5 and 28% ± 3.8 cardiac looping defects for CR#1 and CR#2, respectively (Fig. 1G). Similarly, when we injected a morpholino oligo (MO) to deplete Cfap45, we detected 18% ± 6.2 cardiac looping defects (Fig. 1F and G, Supp Fig1). To test if *cfap45* influences global LR axis formation, we then analyzed the expression of the transcription factor *pitx2c,* which is expressed in the left lateral plate mesoderm and regulates the internal organ *situs* (Lin et al., 1999; Yoshioka et al., 1998). We again depleted *cfap45* using CRISPR or MOs and raised tadpoles to st.28–31. These tadpoles exhibited 21%–38% abnormalities in *pitx2c* expression compared to 6% in uninjected controls and only 5% in Cas9-only injected controls (Fig. 1H and I, Supp Fig1).

3.3. Cfap45 depletion leads to abnormal cilia in the Left-Right Organizer

In the LRO, motile cilia generate leftward fluid flow, activating Nodal signaling only on the left, which propagates to the left lateral mesoderm to instruct the asymmetric gene expression (Blum and Vick, 2015; Sempou and Khokha, 2019). Having established that *pitx2c* expression was abnormal when *cfap45* was depleted, we next examined the LRO for expression of the Nodal antagonist *dand5*, which is initially expressed symmetrically in the LRO, then is downregulated on the left due to cilia-driven fluid flow (Fig. 2A, D) (Schweickert et al., 2010; Vonica and Brivanlou, 2007). We evaluated *dand5* expression at two stages: pre-flow at st15 and post-flow at st18. At st15, *dand5* was symmetrical along the LR axis in *cfap45* G0 mutant embryos, similar to controls, suggesting that pre-flow LRO patterning was normal (Fig. 2A, B, C). At st18, however, *dand5* remained symmetrical in the *cfap45* G0 mutant embryos, failing to downregulate on the left (Fig. 2E – red arrows, 2F).

Given that leftward ciliary flow is crucial for breaking *dand5* symmetry, we examined the LRO cilia. When we depleted Cfap45 using MO, the size of the LRO was slightly enlarged compared to controls and slightly decreased in the number of total cilia, cilia per area, and cilia length (cilia count: control 201 ± 16 vs. morphant 187 ± 37; LRO area: control 3.174

$\mu m^2 * 10^4 \pm 0.41$ vs. morphant 3.550 $\mu m^2 * 10^4 \pm 0.37$, cilia length: control 5522 nm±792 vs. morphant 4464 ± 813) (Fig. 2G–L). Interestingly, we detected significant morphological abnormalities when closely examining the cilia morphology. Cilia were often thick, curved, and bulging around the axoneme (Fig. 2H, white arrows). The abnormalities in *pitx2c* and *dand5* expression combined with this abnormally shaped monocilia suggested that cilia signaling at the LRO was defective.

3.4. Cfap45 depletion impairs cilia-driven fluid flow on the Xenopus epidermis

Given the structural defects in LRO monocilia and the history of the patient with recurrent respiratory infections, we wondered whether cilia in the epidermal multiciliated cells (MCCs) would also be affected. At stages 25–32, the *Xenopus* epidermis is populated with polarized motile MCCs, which create fluid flow from head to tail, clearing the epidermal surface of bacteria and other pathogens, similar to the mammalian respiratory tract. We and others have previously shown that this cilia-driven epidermal flow can be assayed by Optical Coherence Tomography (OCT) imaging (Tang et al., 2019; Huang et al., 2015). When we depleted *cfap45* using our CRISPRs or MO, we detected significant abnormalities in epidermal cilia-driven fluid flow, either slow or undetectable by OCT imaging (Fig. .3A–E, Movie 1). We then sorted these tadpoles as normal-flow, slow-flow, and no-flow phenotypes. Next, we detected extensive cilia loss in slow-flow and no-flow using immunofluorescence staining with an antibody against acetylated tubulin to mark the cilia and phalloidin to mark the actin (Fig. 3G). Interestingly, the cilia looked short, deformed, and markedly reduced in numbers, consistent with OCT imaging findings (Fig. 3G, Supp Fig1).

3.4.1. Cfap45 is required for cilia stability in Xenopus—To better understand the mechanism of ciliary malformation, we used live confocal imaging to examine ciliogenesis in *cfap45* depleted tadpoles. At stage 28, cilia appeared normal grossly and were beating. However, unlike control MCCs (Fig. 4A), they quickly began to curl, forming circular structures at the tip and exhibiting bulging along the axoneme (Fig. 4B and C). The ciliary deformation almost always starts at the tip, the plus end of the microtubules, self-folding and forming a circular shape (Fig. 4D–F). Interestingly, despite these structural abnormalities, they were still motile, although they could not generate extracellular fluid flow (Movie 2,3). In addition, a portion of the cilium detached from the surface, leading to free-floating cilia fragments above the cells (Fig. 4G – yellow circle), while the residual cilium retracted and curled.

We performed transmission electron microscopy (TEM) at the stages when cilia become unstable based on our live imaging to examine the ultrastructural changes within the axoneme. In wild-type tadpoles, a cross-section of the cilium reveals a 9 + 2 doublet microtubule structure with outer/inner dynein arms and connective proteins (Fig. 4H). When *cfap45* is depleted, the axoneme is disrupted, microtubule organization is abnormal, and dynein arms are occasionally missing (Fig. 4I, Supp Fig2), resembling cilia degeneration. In summary, *cfap45* depletion in *Xenopus* led to malformed mono- and multi-cilia leading to LR patterning defects and loss of epidermal cilia flow.

3.5. The patient variant is a loss-of-function

The patient had a homozygous L522P variant in CFAP45; however, the functional relevance of this variant was uncertain. For this experiment, we used two-cell injections in *Xenopus*. By microinjecting into one cell at the two-cell stage, we can select embryos in which either the left or right side of the embryo is targeted for knockdown and use the other side as an internal control. In this setting, we injected MO at the one-cell stage to deplete Cfap45 throughout the embryo, and then at the two-cell stage, we injected wild-type human *CFAP45* mRNA traced with membrane RFP in just one of the two cells. In this way, we can determine if wild-type human CFAP45 can rescue cilia by comparing one side of the embryo to the other side as an internal control (Fig. 5A). At st32, we labeled cilia with an anti-acetylated tubulin antibody. As expected, we observed a loss of cilia on the MO-only side, while on the side co-injected with human *CFAP45* mRNA, we detected nearly normal cilia (Fig. 5B–C, Supp. Fig3). We then repeated the experiment with the p.Leu522Pro-*CFAP45*-mRNA patient variant, which failed to rescue, suggesting that the patient variant has impaired function (Fig. 5D–E–Supp. Fig3). We also conclude that our depletion strategies are specific and effective based on multiple criteria. First, depletion phenotypes are similar across different methodologies (MO and CRISPR), including two non-overlapping sgRNAs. Second, we detect gene modification at the expected sites with G0 CRISPR (Supp. Fig3). Finally, we can rescue our MO phenotype with wild-type human mRNA but not the patient variant (Supp. Fig3).

Furthermore, to investigate Cfap45 expression, we fused GFP to the N-terminus of the human wild-type human *CFAP45*. To test whether the GFP-tagged CFAP45 is relevant physiologically, we assayed whether the GFP-CFAP45 construct could rescue cilia in morphants. Again, we used two-cell injections, where we injected MO at the one-cell stage and GFP-*CFAP45* into one cell at the two-cell stage (Fig. 5F–G). Indeed, GFP-*CFAP45* rescued cilia suggesting that the GFP-*CFAP45* construct is functional (Supp. Fig3).

3.6. Cfap45 is localized to the ciliary axoneme and base in multiciliated cells on the Xenopus epidermis

Both monocilia and multicilia assemble through several steps. First, centrioles duplicate and migrate to the apical region of the cell, where they eventually dock to the apical cell membrane and then mature into basal bodies (Stubbs et al., 2006). In order to identify how *cfap45* may affect cilia stability and structure, we sought to understand where Cfap45 localizes at the cilia (if at all). We labeled the ciliary membrane by injecting membrane RFP and co-injected GFP-*CFAP45*. GFP-CFAP45 localizes to the ciliary axoneme and the cilium base in *Xenopus* MCCs (Fig. 6A). Interestingly, GFP-CFAP45 was not uniformly distributed along the axoneme and instead appeared in a punctate pattern (Fig. 6B–C, Movie 4,5). Next, we co-labeled cilia in wild-type embryos with antibodies against Cfap45 and acetylated tubulin. We confirmed that Cfap45 was localized to the MCCs and had a punctate periodic pattern along the axoneme length, recapitulating the GFP-CFAP45 expression (Fig. 6D–G). When we deplete CFAP45 using MOs, we observe the reduction of the signal (Supp Fig4). On the *Xenopus* epidermis, multiciliated cells (MCCs) harbor an apical actin network where basal bodies dock to the center of an actin lattice. When we injected Cherry -*CFAP45* mRNA at the one-cell stage and raised the tadpoles to st32, CFAP45 localized

to the center of the actin lattice and the ciliary axoneme (Fig. 7A, Movie 6). To examine Cfap45 localization at the cilium base, we injected GFP-*CFAP45* mRNA with a known basal body marker, *centrin* RFP mRNA. Cfap45 and Centrin colocalized at the base of the cilia suggesting that Cfap45 localizes to the basal body (Fig. 7B). Together, these experiments demonstrated that Cfap45 is expressed along the axoneme in a punctate pattern and at the base of the cilium.

3.7. Cfap45 is stationary along the axoneme

During ciliogenesis, microtubules project out of the cell from basal bodies to form the ciliary axoneme. Cilia lack the machinery for protein synthesis; therefore, axonemal assembly and maintenance depend on intraflagellar transport (IFT) proteins, which constantly deliver proteins from their site of synthesis in the cytoplasm to the axoneme (Kozminski, 1995; Kozminski et al., 1993, 1995; Pazour et al., 1999). The punctate expression pattern of Cfap45 along the axoneme is reminiscent of these IFT particles (Brooks and Wallingford, 2012). To identify if Cfap45 co-localizes with these IFT proteins, we injected *IFT80*-GFP mRNA and Cherry-*CFAP45*- mRNA at the one-cell stage and raised tadpoles to st32. We imaged the cilia of the *Xenopus* MCCs with a Bruker Opterra confocal swept field fluorescent microscope. This microscope is designed to excite and collect two independent channels concurrently using two EMCCD cameras. As expected, the IFT80-GFP particles are visible at the base of the cilia and the ciliary axoneme (Fig. 7C – Movie 6, 7). We assessed IFT protein movement along the axoneme, where we plotted the intensity of the IFT80-GFP signal along a line drawn from the base of the cilium to the tip (the single cilium analyzed is boxed with a yellow rectangle- Fig. 7D) to create a kymograph, where time is plotted along the y-axis and the GFP intensity along the cilium for each time point plotted along the x-axis. The localization of the IFT protein (presented as dark lines) changes along the x-axis. In Fig. 7G, multiple particle tracks were visible (black lines), and one of the IFT protein movements was tracked with black arrows. The simultaneously recorded Cherry-CFAP45 (Fig. 7E–F, Movie 6), unlike IFT80, did not show any movement (Fig. 7H), indicating that Cfap45 is a static, interspersed, repetitive protein within the axoneme. Finally, when we mutate *cfap45* with CRISPR, as the cilia degenerate, IFT80 trafficking is compromised (Movie 8).

4. Discussion

Using whole-exome sequencing in a consanguineous family by our analysis, with two siblings with heterotaxy syndrome, we identified a novel homozygous recessive variant in *CFAP45* (cilia and flagella associated protein 45, also known as *CCDC19*, coiled-coil domain-containing protein 19).

Our work illustrates that *cfap45* regulates left-right patterning in *Xenopus,* recapitulating our patients' heterotaxy phenotype. We show that when *cfap45* is depleted, tadpoles have defects in cardiac looping as well as in key global markers of LR patterning: *pitx2c* and *dand5*. Given defects in these LR markers, we examined cilia in the LRO of *cfap45* depleted tadpoles and discovered they were abnormal. Since cilia are essential for LR patterning, we suspect that these abnormal cilia fail to break LR symmetry leading to the *situs* defects in

the embryos, providing a plausible mechanism for heterotaxy in the patients. Previous work also suggests that in heterotaxy patients, ciliary defects may affect both the multiciliated epithelium of the respiratory tract and the monocilia of the LRO (Stewart et al., 2018). Indeed, we show that Cfap45 is indispensable for monociliated and multiciliated cells. Our clinical findings align well with the recent report describing mutations in *CFAP45* in three patients with heterotaxy and asthenospermia consistent with ciliopathy (Dougherty et al., 2020). Together, there is substantial evidence to support a role for CFAP45 in left-right patterning. However, the biological function of CFAP45 is uncertain.

A recent report indicates that CFAP45 affects '*cilia motility*' via an adenine nucleotide homeostasis module regulating the outer dynein arms (Dougherty et al., 2020). In this work, Daughtery et al. used a 772-gene cilia proteome panel to characterize motile ciliopathy cases and identified *CFAP45* as a motile ciliopathy gene. Similar to our findings in *Xenopus,* CFAP45 was located in the axoneme in mouse and porcine respiratory cilia by IHC. CRISPR/Cas9-based mice lacking exon 3 of *Cfap45* −/− offspring exhibited a motile ciliopathy phenotype where the littermates were infertile and demonstrated hydrocephalus, further consistent phenotypes associated with ciliopathies. Their analysis showed no ultrastructural defects in planarian *Schmidtea mediterranea*, *Cfap45*$^{-/-}$ mice, or the respiratory cilia from patients, yet the proteomic link of CFAP45 to adenylate kinase AK8, ADP homeostasis, and dynein ATPases suggested a role in cilia motility. However, two reports on *Chlamydomonas* suggest that CFAP45 has a role in '*cilia stability*' rather than cilia motility (Owa et al., 2019; Ma et al., 2019). Using single-particle cryo-electron microscopy in *Chlamydomonas* (Ma et al., 2019), Cfap45 is located at the luminal surface (inner surface) of the microtubules (microtubule inner proteins MIPs), which are believed to stabilize the axoneme and resist mechanical forces created by the ciliary beating (Owa et al., 2019; Nicastro et al., 2006; Ishikawa, 2017). The core of motile cilia consists of nine doublet microtubules, which comprise 13 protofilaments (A-tubule) and an incomplete 10 protofilaments (B-tubule). Biochemically, Cfap45 binds to the inner lumen of the B-tubule and bundle protofilaments that stabilize doublet microtubules in the cilia axoneme (Owa et al., 2019; Ma et al., 2019).

Our findings in *Xenopus* epidermal MCCs suggest that ciliogenesis occurs in *cfap45* depleted tadpoles normally, consistent with all previous reports, but cilia motility is unaffected initially. In our real-time imaging of the epidermal MCCs of the *Xenopus* epidermis, we did not appreciate any motility defects initially, in contrast to Daugherty et al. suggesting that CFAP45 supports ciliary beating. However, as the cilia mature and beating begins, the axoneme becomes unstable in *Xenopus*. We first observe the curling of the cilia at the tips, forming a circular structure, and then eventually, cilia snap at various lengths. Over a short period, the cilia on the entire epidermal surface are shed. Our TEM analysis shows the disorganization along the entire axoneme following this process. Therefore, we conclude that our findings functionally align better with the reports by Owa and Ma (Owa et al., 2019; Ma et al., 2019) where Owa et al. characterize Fap45 as a microtubule inner protein in *Chlamydomonas* and its loss leads to less stable microtubules, similar to our *Xenopus* findings. We show that the loss of extracellular fluid flow over the surface of *cfap45* depleted *Xenopus* results due to the disruption of cilia stability, which aligns with the studies in *Chlamydomonas*.

Furthermore, while we initially thought that the punctate, periodic pattern of Cfap45 along the axoneme resembled IFT particles. In fact, this pattern did not vary with time; rather, it resembled microtubule inner proteins known to have periodicities along the axoneme consistent again with *Chlamydomonas* cryo-EM findings.

5. Conclusion

Overall, our work further provides insight into the mechanism of cilia pathologies seen in our patients with human motile ciliopathies. Future work should focus on the potential interactors of *cfap45* within the ciliary axoneme to further analyze the nature of cilia destabilization in our patients.

Supplementary Material

Refer to Web version on PubMed Central for supplementary material.

Acknowledgments

The authors would like to thank the family who inspired this work. We thank the CCMI core at Yale for confocal and EM imaging.

Funding

This work was supported by NIH R01HD102186 to MKK and R01NS127879 ED.

Data availability

Data will be made available on request.

References

Antony D, et al. , 2013. Mutations in CCDC39 and CCDC40 are the major cause of primary ciliary dyskinesia with axonemal disorganization and absent inner dynein arms. Hum. Mutat 34 (3), 462–472. [PubMed: 23255504]

Basu B, Brueckner M, 2008. Cilia multifunctional organelles at the center of vertebrate left-right asymmetry. Curr. Top. Dev. Biol 85, 151–174. [PubMed: 19147005]

Becker-Heck A, et al. , 2011. The coiled-coil domain containing protein CCDC40 is essential for motile cilia function and left-right axis formation. Nat. Genet 43 (1), 79–84. [PubMed: 21131974]

Bhattacharya D, et al. , 2015. CRISPR/Cas9: an inexpensive, efficient loss of function tool to screen human disease genes in Xenopus. Dev. Biol 408 (2), 196–204. [PubMed: 26546975]

Blum M, Vick P, 2015. Left-right asymmetry: cilia and calcium revisited. Curr. Biol 25 (5), R205–R207. [PubMed: 25734272]

Boskovski MT, et al. , 2013. The heterotaxy gene GALNT11 glycosylates Notch to orchestrate cilia type and laterality. Nature 504 (7480), 456–459. [PubMed: 24226769]

Bowers PN, Brueckner M, Yost HJ, 1996. The genetics of left-right development and heterotaxia. Semin. Perinatol 20 (6), 577–588. [PubMed: 9090782]

Brooks ER, Wallingford JB, 2012. Control of vertebrate intraflagellar transport by the planar cell polarity effector Fuz. J. Cell Biol 198 (1), 37–45. [PubMed: 22778277]

Charrier JB, et al. , 1999. Defining subregions of Hensen's node essential for caudalward movement, midline development and cell survival. Development 126 (21), 4771–4783. [PubMed: 10518494]

Date P, et al. , 2019. Visualizing flow in an intact CSF network using optical coherence tomography: implications for human congenital hydrocephalus. Sci. Rep 9 (1), 6196. [PubMed: 30996265]

del Viso F, Khokha M, 2012. Generating diploid embryos from Xenopus tropicalis. Methods Mol. Biol 917, 33–41. [PubMed: 22956081]

Deniz E, et al. , 2017. Analysis of craniocardiac malformations in Xenopus using optical coherence tomography. Sci. Rep 7, 42506. [PubMed: 28195132]

Deniz E, et al. , 2018. CRISPR/Cas9 F0 screening of congenital heart disease genes in Xenopus tropicalis. Methods Mol. Biol 1865, 163–174. [PubMed: 30151766]

Dougherty GW, et al. , 2020. CFAP45 deficiency causes situs abnormalities and asthenospermia by disrupting an axonemal adenine nucleotide homeostasis module. Nat. Commun 11 (1), 5520. [PubMed: 33139725]

Essner JJ, et al. , 2005. Kupffer's vesicle is a ciliated organ of asymmetry in the zebrafish embryo that initiates left-right development of the brain, heart and gut. Development 132 (6), 1247–1260. [PubMed: 15716348]

Gong Y, Mo C, Fraser SE, 2004. Planar cell polarity signalling controls cell division orientation during zebrafish gastrulation. Nature 430 (7000), 689–693. [PubMed: 15254551]

Hamada H, 2016. Roles of motile and immotile cilia in left-right symmetry breaking. In: Nakanishi T, et al. (Eds.), Etiology and Morphogenesis of Congenital Heart Disease: from Gene Function and Cellular Interaction to Morphology, pp. 57–65. Tokyo.

Hoffman JI, Kaplan S, 2002. The incidence of congenital heart disease. J. Am. Coll. Cardiol 39 (12), 1890–1900. [PubMed: 12084585]

Homsy J, et al. , 2015. De novo mutations in congenital heart disease with neurodevelopmental and other congenital anomalies. Science 350 (6265), 1262–1266. [PubMed: 26785492]

Huang BK, et al. , 2015. Quantitative optical coherence tomography imaging of intermediate flow defect phenotypes in ciliary physiology and pathophysiology. J. Biomed. Opt 20 (3), 030502. [PubMed: 25751026]

Ishikawa T, 2017. Axoneme structure from motile cilia. Cold Spring Harbor Perspect. Biol 9 (1).

Kawasumi A, et al. , 2011. Left-right asymmetry in the level of active Nodal protein produced in the node is translated into left-right asymmetry in the lateral plate of mouse embryos. Dev. Biol 353 (2), 321–330. [PubMed: 21419113]

Khokha MK, et al. , 2002. Techniques and probes for the study of Xenopus tropicalis development. Dev. Dynam 225 (4), 499–510.

Kozminski KG, 1995. High-resolution imaging of flagella. Methods Cell Biol 47, 263–271. [PubMed: 7476498]

Kozminski KG, et al. , 1993. A motility in the eukaryotic flagellum unrelated to flagellar beating. Proc. Natl. Acad. Sci. U. S. A 90 (12), 5519–5523. [PubMed: 8516294]

Kozminski KG, Beech PL, Rosenbaum JL, 1995. The Chlamydomonas kinesin-like protein FLA10 is involved in motility associated with the flagellar membrane. J. Cell Biol 131 (6 Pt 1), 1517–1527. [PubMed: 8522608]

Lane M, Khokha MK, 2022. Obtaining Xenopus tropicalis embryos by in vitro fertilization. Cold Spring Harb. Protoc 2022 (4). Pdb prot106351.

Lek M, et al. , 2016. Analysis of protein-coding genetic variation in 60,706 humans. Nature 536 (7616), 285–291. [PubMed: 27535533]

Lin CR, et al. , 1999. Pitx2 regulates lung asymmetry, cardiac positioning and pituitary and tooth morphogenesis. Nature 401 (6750), 279–282. [PubMed: 10499586]

Ma M, et al. , 2019. Structure of the decorated ciliary doublet microtubule. Cell 179 (4), 909–922 e12. [PubMed: 31668805]

McGrath J, et al. , 2003. Two populations of node monocilia initiate left-right asymmetry in the mouse. Cell 114 (1), 61–73. [PubMed: 12859898]

Narasimhan V, et al. , 2015. Mutations in CCDC11, which encodes a coiled-coil containing ciliary protein, causes situs inversus due to dysmotility of monocilia in the left-right organizer. Hum. Mutat 36 (3), 307–318. [PubMed: 25504577]

Nicastro D, et al. , 2006. The molecular architecture of axonemes revealed by cryoelectron tomography. Science 313 (5789), 944–948. [PubMed: 16917055]

Owa M, et al. , 2019. Inner lumen proteins stabilize doublet microtubules in cilia and flagella. Nat. Commun 10 (1), 1143. [PubMed: 30850601]

Pazour GJ, Dickert BL, Witman GB, 1999. The DHC1b (DHC2) isoform of cytoplasmic dynein is required for flagellar assembly. J. Cell Biol 144 (3), 473–481. [PubMed: 9971742]

Pierpont ME, et al. , 2007. Genetic basis for congenital heart defects: current knowledge: a scientific statement from the American heart association congenital cardiac defects committee, council on cardiovascular disease in the young: endorsed by the American academy of pediatrics. Circulation 115 (23), 3015–3038. [PubMed: 17519398]

Schweickert A, et al. , 2007. Cilia-driven leftward flow determines laterality in Xenopus. Curr. Biol 17 (1), 60–66. [PubMed: 17208188]

Schweickert A, et al. , 2010. The nodal inhibitor Coco is a critical target of leftward flow in Xenopus. Curr. Biol 20 (8), 738–743. [PubMed: 20381352]

Sempou E, Khokha MK, 2019. Genes and mechanisms of heterotaxy: patients drive the search. Curr. Opin. Genet. Dev 56, 34–40. [PubMed: 31234044]

Sifrim A, et al. , 2016. Distinct genetic architectures for syndromic and nonsyndromic congenital heart defects identified by exome sequencing. Nat. Genet 48 (9), 1060–1065. [PubMed: 27479907]

Stewart E, et al. , 2018. Airway ciliary dysfunction: association with adverse postoperative outcomes in nonheterotaxy congenital heart disease patients. J. Thorac. Cardiovasc. Surg 155 (2), 755–763 e7. [PubMed: 29056267]

Stubbs JL, et al. , 2006. Radial intercalation of ciliated cells during Xenopus skin development. Development 133 (13), 2507–2515. [PubMed: 16728476]

Tang T, et al. , 2019. Gaussian process post-processing for particle tracking velocimetry. Biomed. Opt Express 10 (7), 3196–3216. [PubMed: 31360598]

Vonica A, Brivanlou AH, 2007. The left-right axis is regulated by the interplay of Coco, Xnr1 and derriere in Xenopus embryos. Dev. Biol 303 (1), 281–294. [PubMed: 17239842]

Yoshiba S, et al. , 2012. Cilia at the node of mouse embryos sense fluid flow for left-right determination via Pkd2. Science 338 (6104), 226–231. [PubMed: 22983710]

Yoshioka H, et al. , 1998. Pitx2, a bicoid-type homeobox gene, is involved in a lefty-signaling pathway in determination of left-right asymmetry. Cell 94 (3), 299–305. [PubMed: 9708732]

Zaidi S, et al. , 2013. De novo mutations in histone-modifying genes in congenital heart disease. Nature 498 (7453), 220–223. [PubMed: 23665959]

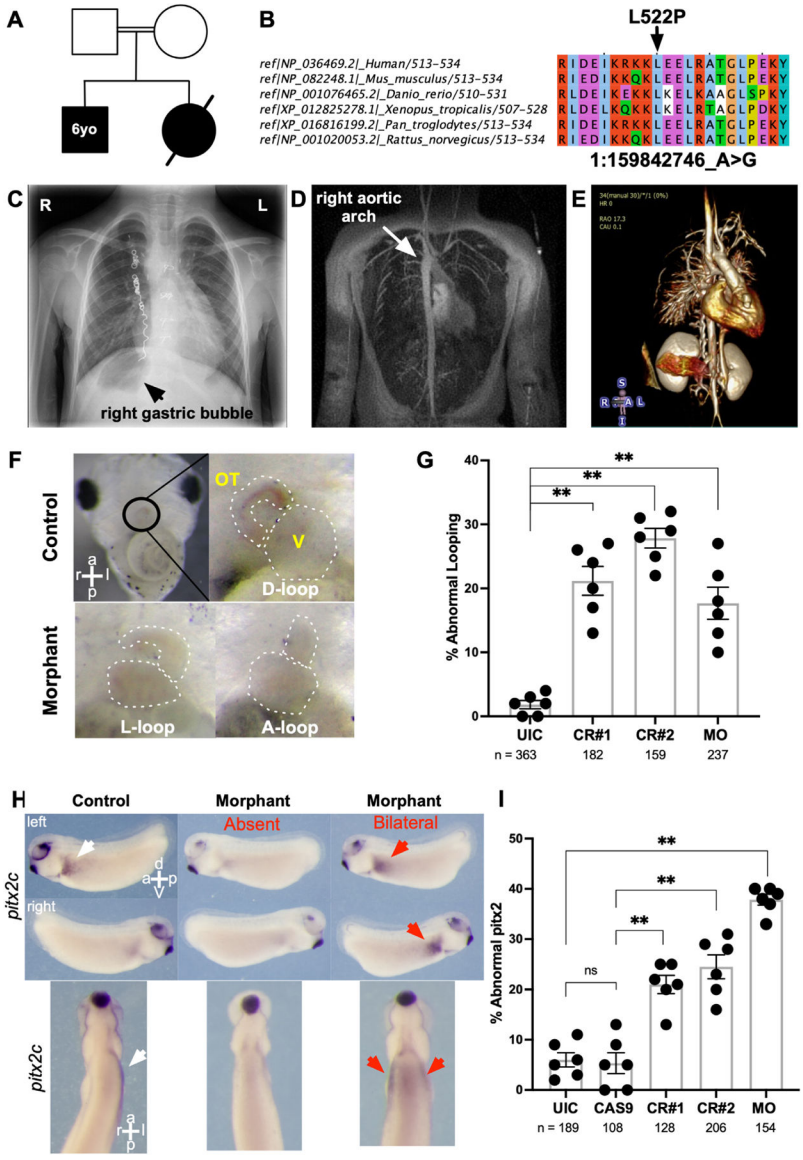

Fig. 1.

cfap45 loss-of-function in humans and *Xenopus* leads to heterotaxy phenotype (**A**) Family pedigree showing the affected 6yo patient and the similarly affected sibling who died at 25 days of life. (**B**) Multiple alignments around the patient variant L522P demonstrate a remarkable degree of conservation of amino acids. (**C**) Chest X-ray shows the right gastric bubble. (**D**) CT-scan of the chest and (**E**) 3D reconstruction shows the right aortic arch indicating abnormal left-right patterning (**F**) The first row shows the tadpole heart in uninjected control (D-loop), and the second row shows the morphant with abnormal (L and A-loop) looping states at stage 46 *Xenopus* heart. The cardiac sac is magnified, the outflow tract border and the ventricle are outlined in white. OT: outflow tract; Ventricle. (**G**) The graph represents abnormal looping percentages in G0 mutants (Crispr#1, Crispr#2) and morphants. Each point represents one experimental group. (**H**) *cfap45* knockdown leads to *pitx2c* abnormalities. The first column shows normal *pitx2c* expression in the left

lateral mesoderm and is absent on the right of stage 28–31 *Xenopus* embryos, highlighted with a white arrow. The second and third columns show abnormal *pitx2c* expression as absent or bilateral, highlighted with red arrows following MO mediated c*fap45* depletion. (I) The graph represents abnormal *pitx2c* expression percentages in G0 mutants (Crispr#1, Crispr#2) and morphants. Each point represents one experimental group. D: dextro, L: levo, A: ambiguous. *p < 0.05, **p < 0.01, ***p < 0.001, ****p < 0.0001.

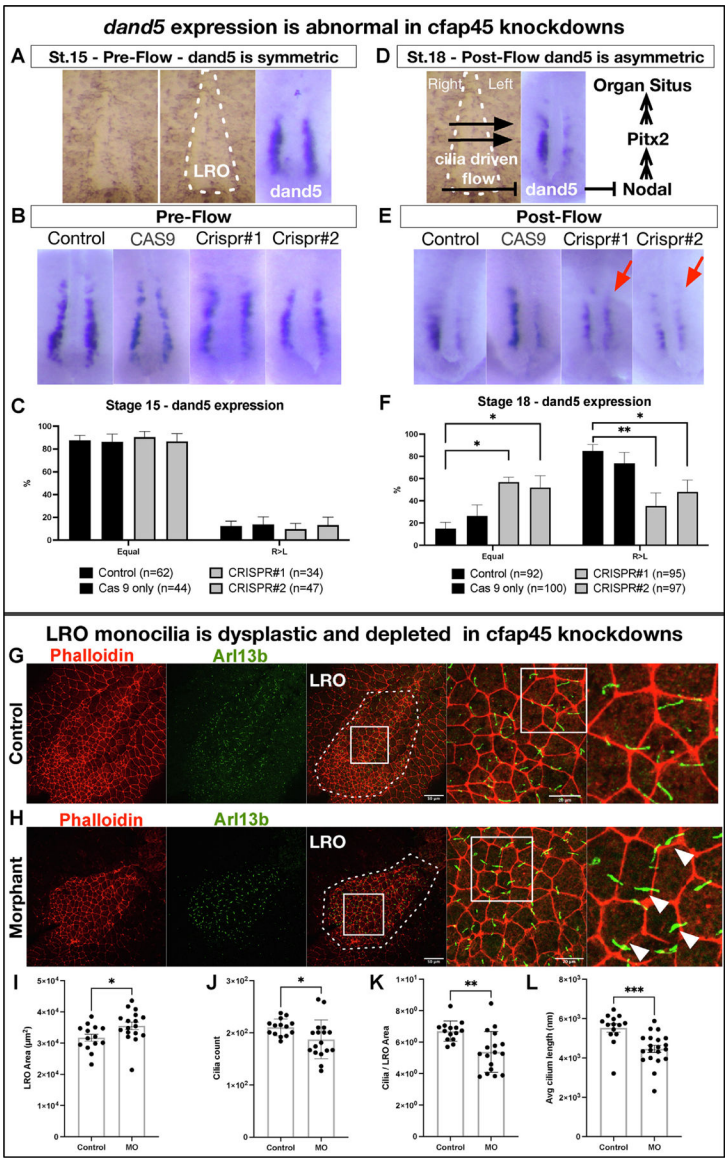

Fig. 2.

cfap45 knockdown causes abnormal *dand5* expression and defects in LRO cilia (**A**) *dand5* is expressed bilaterally symmetrical in the LRO at stage 15 (pre-flow). (**B**) Pre-flow, normal bilateral expression of *dand5 was* observed in G0 mutants compared to uninjected or only CAS9 injected controls. (**C**) Percentages of normal (equal) and abnormal (R > L) *dand5* expression in stage 15 (pre-flow) LROs. G0 mutants show no difference compared to uninjected and Cas9 injected controls. n = number of embryos. (**D**) At stage 18, right to left cilia-driven fluid flow has emerged, suppressing dand5 expression on the left side of the LRO. (**E**) Post-flow, normal reduced left side expression in uninjected and Cas9 injected controls show up as abnormal bilateral expression in G0 mutants indicated with red arrows. (**F**) Percentages of normal (R > L) and abnormal (equal) *dand5* expression in stage 18 (post-flow) LROs. A significant number of G0 mutants show abnormal bilateral *dand5* expression compared to uninjected and Cas9 injected controls—n = number of embryos.

(**G–H**) LROs stained with phalloidin to label cell borders and anti - Arl13b antibody to label monocilia. The white dashed line indicates the LRO area. LRO monocilia were malformed and lost in morphants, also showing bulging at the tip and midshaft of the cilia, indicated by white arrows. White squares indicate the magnified areas (**H**). LRO area is slightly enlarged (**I**), and cilia numbers (**J**), cilia per LRO area (**K**), and cilia length are reduced in morphants. MO: Morpholino oligo, LRO: Left-right organizer.*$p < 0.05$, **$p < 0.01$.

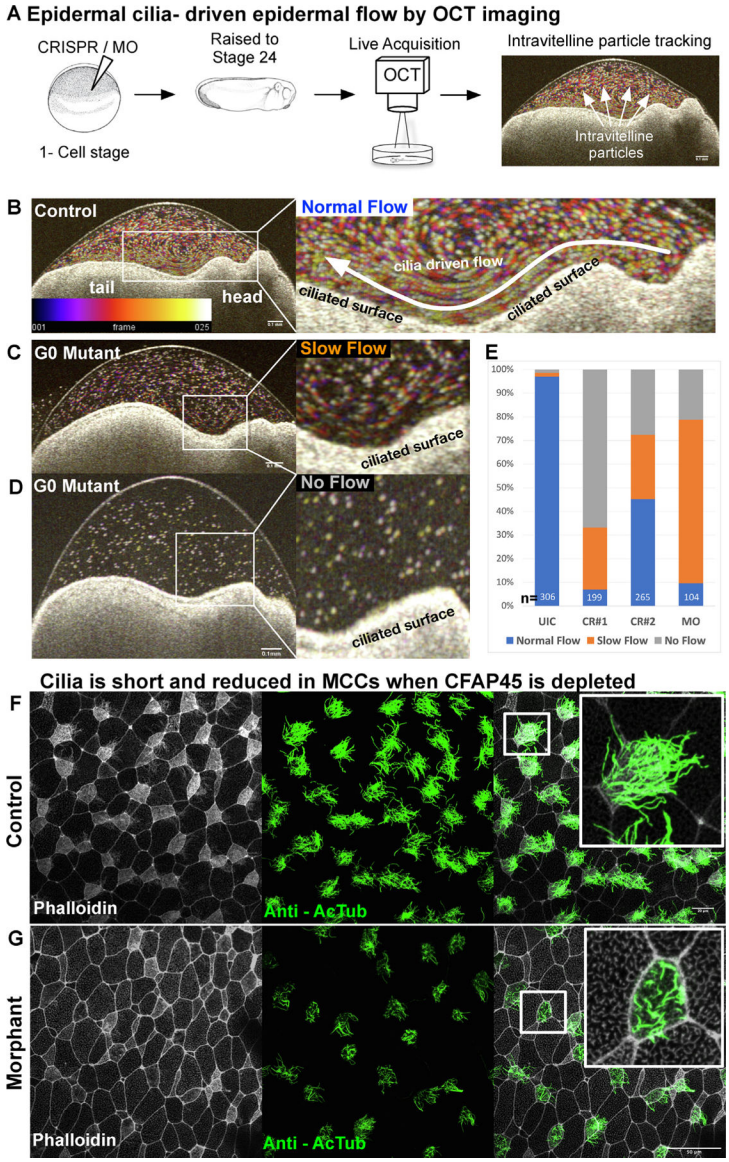

Fig. 3.

cfap45 knockdown causes abnormalities in cilia-driven epidermal flow and leads to defects in epidermal multicilia. (**A**) Epidermal multicilia beating is planarly polarized, generating head-to-tail fluid flow along the surface. This flow can be visualized using Optical Coherence Tomography (OCT) imaging, where intravitelline endogenous particle movements can be tracked *in vivo* (Movie1). (**B–E**) We obtained real-time OCT movies and, using 25 frames, built particle trajectories with ImageJ. Temporal color coding depicts particle trajectory over time. The color bar represents color versus the corresponding frame number in the color-coded image. Based on the trajectory map over 25 frames, we classified the flow as normal (**B**), slow (**C**), or absent (**D**). When *cfap45* is depleted, the epidermal flow is significantly slower or stationary. (**E**) Based on OCT imaging, percentages of embryos with normal, slow, and no-flow in uninjected controls and *cfap45* depleted tadpoles —n = number of embryos. (**F–G**) Cilia are lost in multiciliated cells (MCCs) when Cfap45

is depleted with MO. Epidermal MCCs marked with anti-acetylated-tubulin (green) for cilia and phalloidin (white) for actin.

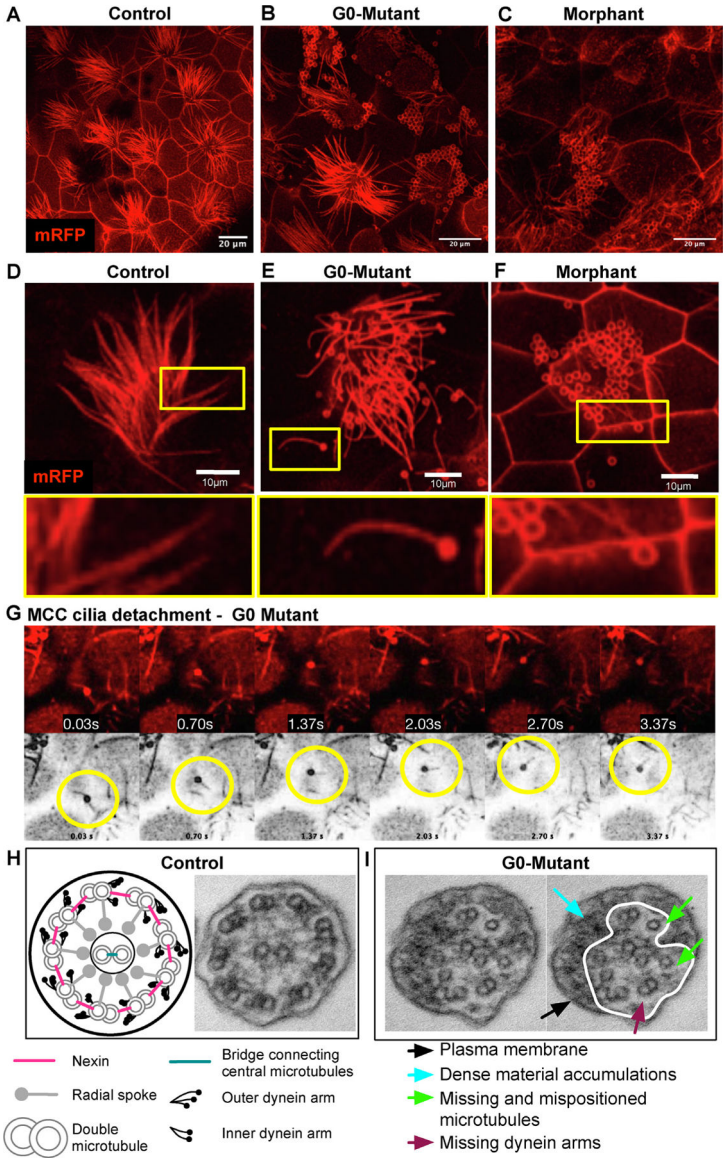

Fig. 4.

Epidermal MCCs demonstrate axonemal disorganization and instability when *cfap45* is knocked down (**A–C**) Wide-field images of the Epidermal MCCs marked with membrane RFP in controls (**A**), G0 mutants (**B**), and morphants (**C**). When *cfap45* is depleted, most MCCs display curled and shortened cilia (Movie 2,3). (**D-F**) Focused and magnified MCC images in control (**D**), G0 mutants (**E**), and morphants (**F**) show curling of the cilia leading to shortening and suggesting that the deformation leads to detached cilia. (**G**) Montaged images from live G0 mutant epidermal cilia imaging show the detached, free-floating cilium. The bottom row is colored black and white to track better the detached cilium encircled in yellow. (**H**) Electron Microscope image of the transverse section of the epidermal MCC shows 9 + 2 microtubule organization. A pair of microtubules is surrounded by nine pairs connected with radial spokes. This organization is abnormal when *cfap45* is depleted using CRISPR.

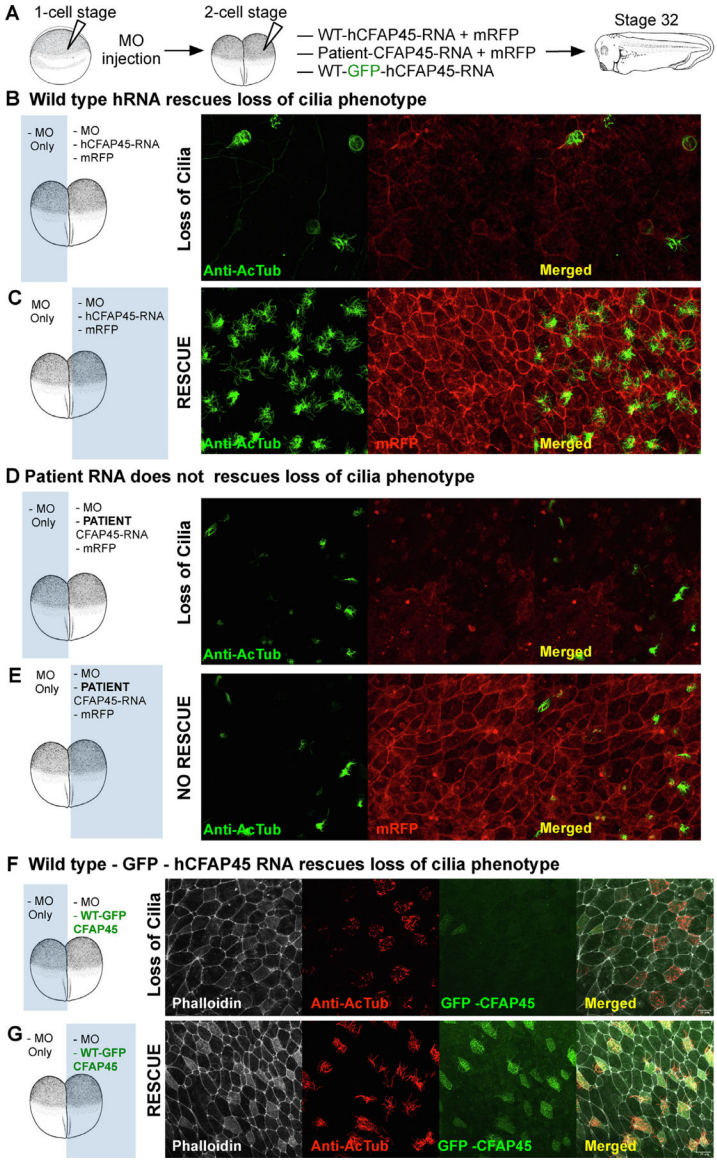

Fig. 5.

Wild-type human *cfap45* mRNA rescues loss of cilia phenotype, whereas the patient variant fails (**A**) Experimental setup. First, morpholino is injected at the one-cell stage, followed by human RNA (WT or patient variant) with membrane RFP tracer injection at the two-cell stage. Then, we raised tadpoles to stage 32 to assess epidermal MCCs. (**B**, **D**, **F**) Depletion of Cfap45 by MO results in MCC loss. (**C**) Wild-type RNA injection at the two-cell stage traced with membrane RFP shows the recovery of the MCCs on the injected side. (**E**) RNA with patient variation injections traced with membrane RFP fails to recover loss of cilia in MCCs. (**G**) Wild-type GFP-hCFAP45 RNA injection at the two-cell stage shows the recovery of the MCCs on the injected side. Phalloidin was used to label actin to show cell borders, and an anti-acetylated α-tubulin antibody was used to label cilia.

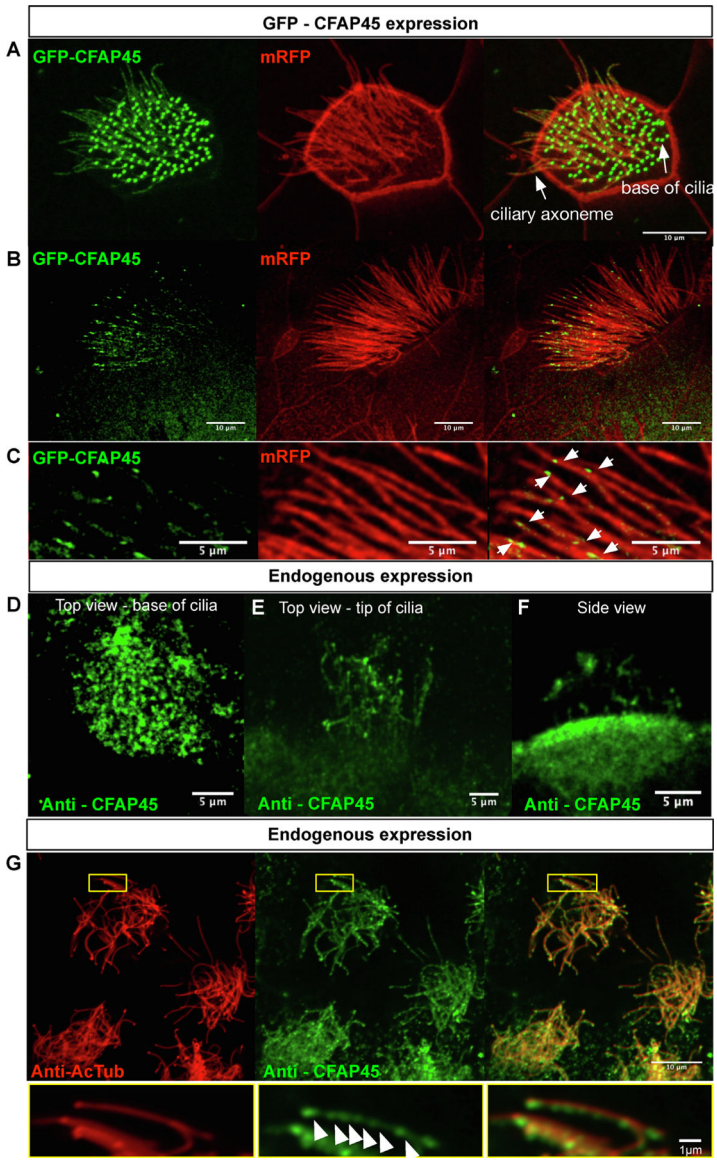

Fig. 6.

Cfap45 localization in *X.tropicalis* MCCs (**A–C**) *X. tropicalis* epidermis expressing GFP-CFAP45 and membrane RFP. (**A**) Focus is concentrated on the base of the cilia where GFP-CFAP45 is expressed, (**B**) Focus is concentrated on the cilia showing the dotty localization along the axonemes. (**C**) Magnified views. White arrows highlight GFP-CFAP45 localization. (**D–F**) *X. tropicalis* epidermal MCCs labeled with anti-CFAP45. (**D**) Top view focusing on the base of the cilia at the apical surface. (**E**) Top view focusing on the cilia axonemes. (**F**) Side view showing apical surface and cilia staining. (**G**) *X. tropicalis* epidermal MCCs labeled with anti-acetylated α-tubulin (red, cilia) and anti-CFAP45 (green). Anti-CFAP45 staining pattern is identical to the GFP-CFAP45 expression, showing CFAP45 localization to the cilia in a dotty fashion in the magnified views along the bottom (white arrows).

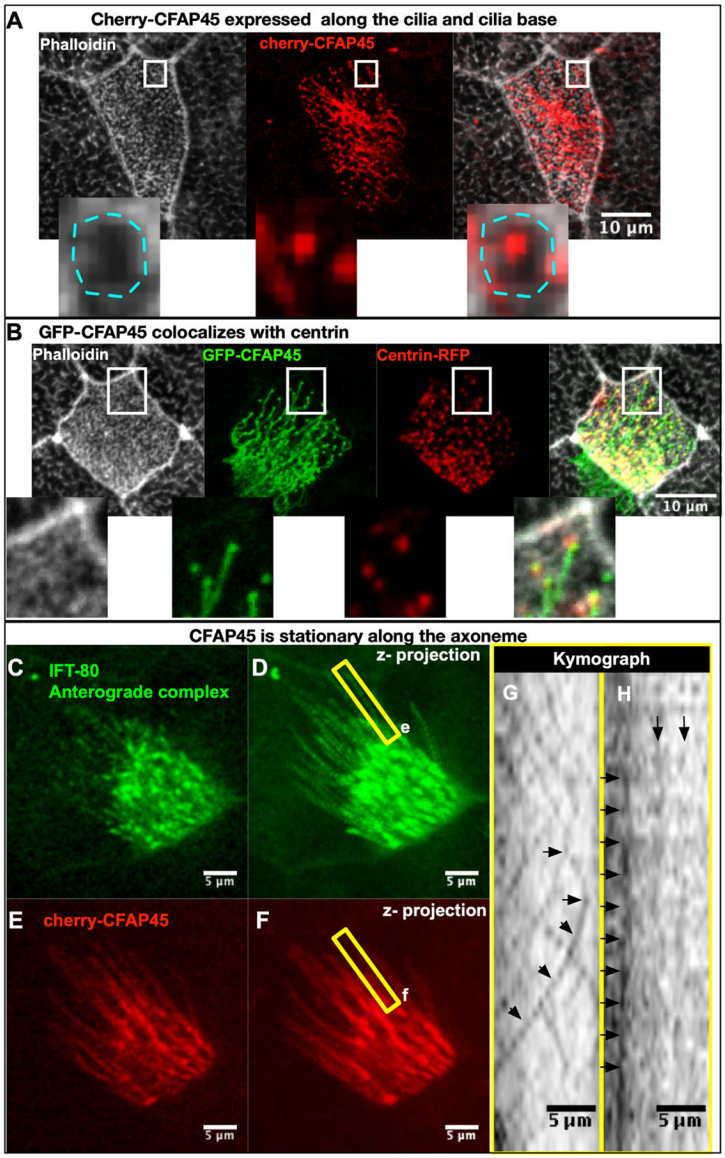

Fig. 7.

CFAP45 localized to the base of the cilia and the ciliary axoneme and, unlike IFT80 protein, is stationary within the cilia. (**A**) **Cherry** - CFAP45 expressed in the epidermal MCCs. Actin in MCCs stained with phalloidin (grey) delineates the cell borders and the apical actin network where the base of the cilia is located at the center. The magnified view delineates the circular actin network (blue). CFAP45 is enriched at the base of the cilia and situated in the center of the apical network. (**B**) GFP- CFAP45 expressed in MCCs and colocalized with Centrin at the base of the cilia. (**C**) IFT-80-GFP expressed in MCC. (**D**) z-projection of fifty frames. (**E**) CFAP45-Cherry expressed in MCC. (**F**) z-projection of fifty frames. (**G**) Kymograph presents the movement of the IFT80-GFP proteins along the single cilium. Multiple lines represent multiple IFTs. As the protein travels, intensity displaces along the cilium forming tracks over time. One particle tracked over time was marked with black arrows. (**H**) Kymograph presents stationary CFAP45-cherry protein. As no movement is

observed, multiple straight lines form over time, representing the non-uniform punctuated pattern of *cfap45*. (Yellow rectangle encloses the single cilium analyzed.)